Catalysis Science & Technology

Accepted Manuscript

ROYAL SOCIETY OF CHEMISTRY

www.rsc.org/catalysis

Facile Synthesis of Ag/MoS_2 Nanocomposite Photocatalyst for Enhanced Visible-Light Driven Hydrogen Gas Evolution

A. J. Cheah[1], W. S. Chiu[1*], P. S. Khiew[2], H. Nakajima[3], T. Saisopa[3,4], P. Songsiriritthigul[3,4], S. Radiman[5], M. A. A. Hamid[5]

[1]Low Dimensional Materials Research Centre, Physics Department, Faculty of Science, University of Malaya, 50603 Kuala Lumpur, Malaysia.

[2] Division of Materials, Mechanics and Structures, Faculty of Engineering, University of Nottingham Malaysia Campus, 43500, Semenyih, Selangor, Malaysia

[3]Synchrotron Light Research Institute, Nakhon Ratchasima 30000, Thailand.

[4]NANOTEC-SUT Center of Excellence on Advanced Functional Nanomaterials and School of Physics, Suranaree University of Technology, Nakhon Ratchasima 30000, Thailand.

[5]School of Applied Physcis, Faculty of Science and Technology, Universiti Kebangsaan Malaysia, 43600 UKM Bangi, Selangor Darul Ehsan, Malaysia.

*Corresponding author: W.S.Chiu (*Tel: +6019-3292772; email:w.s.chiu@um.edu.my*)

Abstract

Current study reports the facile synthesis of Ag/MoS_2 nanocomposite photocatalyst for visible-light driven hydrogen gas evolution. The MoS_2 nanoflakes were hydrothermally prepared and then decorated with Ag nanoparticles (NPs) by simple chemical reduction process at room temperature. Detailed characterizations had been carried out to probe the physical structure and properties of the as-synthesized nanocomposite. The nanocomposite shows enhanced visible-light absorption and pronounced quenching of photoluminescence intensity as compared to that of pure MoS_2. The photocatalytic hydrogen gas evolution experiments reveal that the Ag NPs can act as efficient co-catalyst for MoS_2 nanoflakes and subsequently improve the hydrogen gas evolution rate. Ag-loading dependent photocatalytic tests indicate that the 20 wt%-Ag/MoS_2 nanocomposite exhibits the highest photocatalytic activity with hydrogen gas evolution of 179.5 μmol H_2/g_{cat}, which is enhanced by 95% if compared to that of commercial MoS_2 nanopowder (92.0 μmol H_2/g_{cat}). The

possible mechanisms that contribute to the improvement of visible-light driven photocatalytic performance for nanocomposite are proposed.

1 Introduction

For last two decades, significant efforts have been devoted in the processing of photocatalyst nanomaterials with the aim to be used for heterogeneous photocatalysis process in producing hydrogen gas through water splitting reaction. Although this field has been literally exploded, however, the process efficiencies remain unsatistified.[1] Lately, 2D-MoS_2 nanostructures have become the notion of research due to its anomalous electronic and catalysis performance.[2-4] Recent advancement in hydrogen gas production through water splitting reaction indicates the exceptional catalytic performance of MoS_2 in disassociating water molecules due to its highly-exposed surface area and abundance of active edges. Most of the findings have proof that active edges are the main factors that dictate the overall photocatalytic performance.[5]

Despite of this, latest report lodged by Yu et al. have demonstrate that the electrocatalytic activity of MoS_2 are strictly dependent on the thickness instead of number of active edges.[6] They counterpoint that the hydrogen gas evolution is reduced by a factor of ~4.47 with respect to the addition of every single layer due to additional potential barrier of 0.119 V is required for electron hopping along vertical direction. For the moment, most of the approaches are realized through electrocatalysis reaction, where the overpotential requires more energy than thermodynamically expected to drive water splitting reaction with the supplied of electricity as energy input to initialize the process. Hence, the process still remains a great challenge to be practiced since the efficiency would be lower than the stipulated standard after the electricity energy that being supplied is taken into accounted. On the other hand, for suspension-based photocatalysis reaction, there is no any electrical energy needed to be supplied to initialize the process. Instead, the excitons that formed upon absorbing incident photon can further split the water molecules into its constituents. Therefore, photocatalysis hydrogen

generation through suspension remain attractive since it is well-complement with the worldwide initiative toward the implementation of the technology, which is anticipated to fully harness the sunlight from mother nature as one of highly abundance natural resource.

As part of two-dimensional materials, graphene also has gained significant popularity for photocatalysis applications, where it has been greatly used as matrix that is able in prolong the charge-carrier lifetimes.[7] In contrast to the graphene, MoS_2 appear to be a semiconductor by itself and had been repeatedly proved to exhibit tunable bandgap energy that is strictly dependent on the atomic thickness. The bandgap values can be maneuvered from 1.9 eV (direct bandgap) for a single layer MoS_2 nanosheet, down to 1.2 eV (indirect bandgap) for multilayer MoS_2 nanoflakes, in which both of these bandgap are well-correspond to the light absorption in the visible- (450-700 nm) and infrared-region (700-1400 nm), respectively.[8] As a result, MoS_2 would become one of the ideal candidates to be used as visible- and infrared-active optical material for photo-energy engineering including photosplitting of water.

In terms of the structural characteristic, MoS_2 generally exists in expanded two-dimensional sheet-like structure[8, 9]. Such expanded planar nature not only renders highly-exposed surface area for it, but it is also propitious to be employed as a matrix in supporting other inorganic nanoparticles (NPs) to form new class of nanocomposite with value added features that are highly-suitable for specific applications such as in the case of hybrid photocatalyst materials for photocatalytic hydrogen gas evolution. For last few years, various creative designs of advanced photocatalyst nanocomposites have been reported. Among these include coupling of variety types of semiconductor materials with MoS_2 such as in the case of impregnating MoS_2 with graphitic carbon nitride[3] and integrating CdS with MoS_2.[10] The motive lies behind the attempt is to enable abundance of solar-light to be extracted, especially the visible-light spectrum that constitute 43% of real solar-light.[11] In addition to this, it has been elucidated recently that plasmonic NPs of noble metals (silver, gold and platinum) are also very promising to be used as co-catalyst.[12] Upon integration of those co-catalyst onto

photocatalyst semiconductor, the potential barrier at the interface between MoS_2 and co-cocatalyst is largely altered, in which space charge region is created to facilitate the efficient charge separation process that are highly beneficial for photocatalysis performance with enhanced efficiency.[13] Meanwhile, the capability of noble metals in absorbing visible-light through excitation of surface plasmon resonance (SPR) will create an intense and non-homogeneous electric field on the surface of nearby semiconductors. This so-called "plasmonic energy" can serve as additional energy input to the photoexcited-electrons for refraining charge-recombination, while at the same time it generate a plasmonic heating zone in promoting chemical transformation for breaking water molecules.[14]

In current study, Ag/MoS_2 nanocomposite photocatalyst with different wt% of Ag-loading was prepared by in-situ reduction of Ag^+ ion onto MoS_2 nanoflakes at room temperature. To the best of our knowledge, up to dates, the investigation of Ag/MoS_2 nanocomposite has not been reported especially in term of suspension-based hydrogen gas evolution. The as-prepared Ag/MoS_2 nanocomposite was systematically characterized to probe its structural- and optical-properties. Evaluation have been conducted on its efficiency to be used as a nanocomposite photocatalyst for visible-light driven hydrogen gas evolution through water splitting reaction by comparing with the performance of commercialized MoS_2 nanopowder. The result shows that the nanocomposite with 20 wt% Ag-loading exhibits highest photocatalytic performance, in which 95% enhancement is observed if compared to that of commercial MoS_2 nanopowder. The effects of Ag-loading on the light absorption, photoluminescence property and photocatalytic activity were investigated in detailed, and the possible mechanisms that contribute to the improvement of visible-light driven photocatalytic performance for the nanocomposite are discussed. Current work exemplify the potential in designing nanocomposite photocatalyst material by integrating Ag NPs as co-catalyst onto MoS_2 nanoflakes for improved visible-light driven photocatalytic hydrogen gas production, which can serve as one of feasible approaches for the advancement of renewable energy research.

2 Experimental

2.1 Synthesis of Photocatalyst

2.1.1 Synthesis of the MoS_2 Nanoflakes

2.0 mmol Na_2MoO_5 and 10.0 mmol L-cysteine (HO_2CCHCH_2SH) solutions were prepared and transferred into a teflon-lined stainless steel autoclave. The autoclave was heated in the oven at 200°C for 24 hours and cooled to room temperature naturally. The as-obtained product was precipitated by centrifuge with a speed of 4000 rpm. The supernatant was decanted after centrifugation and the MoS_2 nanoflakes in the form of precipitate were re-dispersed in ethanol. The precipitation and re-dispersion process was repeated for twice. Finally, the resultant precipitate was ambient-dried overnight and ready to be used as matrix for deposition of Ag NPs.

2.1.2 Synthesis of Ag/MoS_2 Nanocomposites

The as-synthesized MoS_2 nanoflakes were dispersed in 30.0 mL distilled water that had been loaded with 3.0 µL of hydrazine (1.0×10^{-4} mol). 1.0 M of $AgNO_3$ solution was dropwise added into the MoS_2 suspension under vigorous stirring. The nominal weight ratios of Ag to MoS_2 were 5, 10, 20 and 50 wt%, respectively. Hereafter, the resulting samples were named as 5 wt%-Ag/MoS_2, 10 wt%-Ag/MoS_2, 20 wt%-Ag/MoS_2 and 50 wt%-Ag/MoS_2. The Ag/MoS_2 nanocomposites were purified with the method similar to the nanoflakes. Finally, the precipitate was ambient-dried overnight and characterized.

2.2 Characterization of Photocatalyst

In order to determine the crystallinity and elemental compositions of the samples, X-ray diffraction (XRD) and X-ray photoelectron spectroscopy (XPS) analysis were carried out, respectively. XPS analysis was performed with photoemission spectroscopy (PES) beam line (BL3.2a) at Synchrotron Light Institute (Thailand). A thermo VG Scientific CLAM2 electron spectrometer with maximum photon energy of 600 eV (energy step of 0.1 eV) was used during operation. The

morphology and elemental mapping of the samples were analyzed by using high resolution transmission electron microscope (HRTEM) (JEOL JEM-2100F). Brunauer-Emmett-Teller (BET) surface area measurements were conducted by using Micromeritics ASAP-2020 analyzer. The ultraviolet-visible (UV-Vis) spectrophotometer (Perkin-Elmer Lambda 750 UV-VIS-NIR) and photoluminescence (PL) spectrometer that has been equipped with 325 nm He-Cd laser were used to measure the optical properties of the samples.

2.3 Photocatalytic Activity

The experimental setup for photocatalytic hydrogen gas production was adopted and modified from Galinska et al.[15] The reaction was conducted by mixing 0.0021 g of Ag/MoS_2 nanocomposite with 4.5 mL of deionized water in a quartz cell, which had been loaded with 0.3 M Na_2S and 0.3 M Na_2SO_3 as holes scavengers. A 300-W Xe arc lamp that served as visible-light source was mounted with a beam turner (Newport 66245) that equipped with fins-like heat sink for dissipating excessive heat effectively. A dichroic beam turning mirror (Newport 66219) was placed inside beam turner to reflect the visible light (420-630 nm) and an IR cut-off filter (Edmund Optics 54-516) was mounted on the filter holder (Newport 62020) to chop-off the IR-light. The incident power that contributed by visible-light was measured by Thermal Power Sensors (C-Series, S310C) that was attached to power meter (Thorlabs, PM100D-USD999 2/8/13). The average power was determined to be 0.310 W/cm^2 for the visible-light that fall in the wavelength in between 400-800 nm. The quartz cell was placed 5.0 cm away from the edge of the filter holder. During the course of photocatalytic reaction, the gases evolved were transferred into sample loop by using a peristaltic pump and further quantified by using gas chromatography (GC-Agilent 7890A) that has equipped with a thermal conductivity detector (TCD) gas chromatograph (MS-5A and HayeSep Q columns). The amount of hydrogen gas produced every hour was quantified by integrating with calibration curve. Exactly same experiment

parameter was employed for commercial MoS_2 nanopowder (US Research Nanomaterials, Inc., US2180) and own-synthesized MoS_2 nanoflakes.

3 Results and discussion

3.1 Characterization of MoS_2 Nanoflakes and Ag/MoS_2 Nanocomposites

Fig. 1 XRD patterns of the (a) as-synthesized MoS_2 nanoflakes and (b) 20 wt %-Ag/MoS_2 nanocomposite. (The darkviolet and khaki-solid line at the bottom refers to the standard pattern of MoS_2 and Ag, respectively).

Fig. 1 shows the XRD spectra of the own-synthesized MoS_2 nanoflakes and 20 wt%-Ag/MoS_2 nanocomposite, respectively. It is observed that the spectrum for MoS_2 nanoflakes is partially resolved, where the most dominant peak of (002) plane is clearly visible if compared to the standard pattern of MoS_2 (JCPDS 00-037-1492). However, other peaks appear to be broad and part of the peaks appreciably overlap among each other to form wide-humps as indicated in the 2θ range of 30^o to 50^o and 55^o to 65^o, respectively. Such broad and featureless humps can be attributed to the excessively small domain or partially crystalline nature of the sample.

According to Liu et al., the nature of MoS_2 that appears in sheet-like structure generally renders poor signal reflection due to lower atomic packing density.[16] Furthermore, if the sample appears to have small crystal domain or partially crystalline character, poor and unresolved diffraction will be obtained due to weak interferences of reflected X-ray photon. In order to resolve this matter, they have conducted in-plane XRD scan, where the detector moves in parallel direction relative to the sample surface. Their result clearly reveals the well-resolved peaks other than (002) plane, which implies the truly two-dimensional growth with low number of stacking along the *c*-axis. As compared with their result, the MoS_2 nanoflakes in Fig. 1(a) shows intense reflection for the plane of (002),

which signifies the sample tends to undergo stacking along the *c*-axis resemble to that of bulk sample. Hence, it is deduced that the as-synthesized MoS_2 nanoflakes appear to be in the form of few layers in addition to the expanded two dimensional planar grow. Moreover, this observation is well-complement with most of the earlier studies that adopting hydrothermal approach in the synthesis of MoS_2 nanostructures without post annealing, where partially resolved X-ray patterns are observed as well.[17]

On the other hand, the spectrum and relative intensities for 20 wt%-Ag/MoS_2 nanocomposite (Fig. 1(b)) indicate the presence of three obvious Ag peaks in addition to the characteristic peak of (002) plane that belongs to MoS_2. Upon incorporation of Ag NPs onto MoS_2 nanoflakes, there are no obvious changes on the MoS_2 diffraction pattern and all the major peaks that belong to Ag are clearly observed. However, there are pronounced diffraction signals of Ag NPs owned to its high atomic packing density that capable in reflecting very intense X-ray signal rather than that of MoS_2 nanoflakes. There is a small hump at 2θ of 25°, which may be due to the systematic error arises from excessive X-ray noise that originates from background of the reflected X-ray beam during the process of analysis. Nonetheless, this spectrum still implies that the nanocomposite indeed yield a heterostructure-crystalline without the formation of alloy since it has been confirmed that homogeneous alloying can cause obvious shifts in the diffraction pattern.[18]

Fig. 2 (a) Wide scan for the commercial MoS_2 nanopowder, MoS_2 nanoflakes and 20 wt%-Ag/MoS_2 nanocomposite (b) narrow scan for the Mo 3d, (c) S 2p and (d) Ag 3d (insets of Fig. 2(b) and 2(c) are the resolved spectra after deconvoluted to its constituent state).

Fig. 2(a) depicts the wide scanning profile for the commercial MoS_2 nanopowder, MoS_2 nanoflakes and 20 wt%-Ag/MoS_2 nanocomposite. There is no any significant deviation observed in between them except for 20 wt%-Ag/MoS_2

nanocomposite, where the characteristic peaks that belongs to Ag 3d doublet is present after Ag NPs is decorated onto the MoS_2 nanoflakes. For 20 wt%-Ag/MoS_2 nanocomposite, the chemical compositions remain identical even though after it has been decorated with Ag NPs. It is worth noting that there is an absence of BE around 236 eV that corresponds to Mo^{6+} $2d_{5/2}$ (Fig. 2(a)) which belongs to oxide-based compounds such as MoO_3.[19] This indicates there is no any oxidized-Mo present for those three samples. Hence, it is further confirmed that all the compounds are indeed pure MoS_2 and there is no any oxide as well as other impurities presence in the samples.

The narrow scan is carried out to clearly elucidate the BE for each elements as well as the purity of the compounds (Fig 2(b-d)). According to Fig. 2(b) that correspond to binding energy of Mo, all the samples show doublet of Mo $3d_{5/2}$ and Mo $3d_{3/2}$ that fall at 229.0 eV and 231.9 eV (inset Fig. 2(b)), respectively. This doublet can be assigned to the Mo^{4+} ion that is contained in MoS_2.[20] Meanwhile, Fig. 2(c) also reveals that all the samples have S 2p spectra which are well-fitted with the doublet constituted of 165.0 eV (S $2p_{1/2}$) and 163.5 eV (S $2p_{3/2}$) (inset Fig. 2(c)), where both of these binding energy can be assigned to the bridging S^{2-} and/or apical S^{2-} ligands in MoS_2.[16] With respect to Ag spectrum (Fig. 2(d)) in the 20 wt%-Ag/MoS_2 nanocomposite, the Ag 4d BE can be assigned to the Ag in the zero valence state that equals to 368.2 eV (Ag $3d_{5/2}$) and 374.3 eV (Ag $3d_{3/2}$).[21] This demonstrates that Ag NPs that had been deposited onto MoS_2 nanoflakes preserve its metallic nature without undergo further oxidation. By integrate the peak area of the spectra with the assistance of X-ray photoemission software, the composition of the elements for Mo, S, and Ag in the 20 wt%-Ag/MoS_2 nanocomposite is determined to be 26.1%, 54.6% and 19.3%, respectively.

Fig. 3 (a) Low magnification (30kX) TEM image of the MoS_2 nanoflakes that was suspended on a lacey copper grid. (b) High resolution TEM image (800kX) of MoS_2 nanoflakes that reveals the defect-rich active edges with

discontinued microstructures. (c) Low magnification (30kX) TEM image of 20 wt%-Ag/MoS_2 nanocomposite depicts that Ag NPs are randomly distributed onto MoS_2 nanoflakes. (d) High resolution TEM image (800kX) of the Ag NPs that embedded on the MoS_2 nanoflakes.

Table 1

Average size of Ag NPs that were produced with different wt% of Ag precursor

Fig. 3(a) depicts the TEM micrograph of the free-standing MoS_2 nanoflakes, which have sheet-like morphology with a lateral size of ~500 nm. The partially transparent feature implies that the thin and isolated-sheets are obtained in current synthesis. Meanwhile, HRTEM image along the side of the nanoflakes reveals the well-known active edges, which is the typical characteristic of this material. The interlayer spacing in between active edges is measured to be 0.62 nm, which is well correlate with the *d*-spacing of (002) plane of standard MoS_2 (Fig 3(b)). This reflects that the nanoflakes are stacked alone the *c*-axis, which is in well-agreement with the result of diffractogram. Occasionally, it is found that part of these active edges appear to be discontinued (arrows in Fig. 3(b)), where concurrent distortion and dislocation are presence along the edges. Such observation is similar to the microstructures of vertical aligned MoS_2 thin film that have been grown by high temperature CVD method.[22] Xie et al. who employed hydrothermal method in producing MoS_2 with similar characteristic, have ascribed these microstructures as defect-rich entities that can serve as additional active sites for enhanced electrocatalytic hydrogen gas evolution.[23] In current study, the formation of defect-rich sites is attributed to the binding effect by ion sulfide of L-cysteine molecules which had been adopted as sulfur precursor. It has been proved that sulfide ions can form complex on nanostuctures surface through sulfur bridging.[24] Hence, it is deduced that the ion sulfides are tightly-anchor on the surface of the preform MoS_2 nanoflakes. As a result, the planar growth is

strictly promoted to form two-dimensional flaky-like structure. Under prolong annealing process in hydrothermal condition, the numbers of sulfide ions that anchor on the as-formed nanoflakes surface are increase with respect to the prolong crystallization process. However, excessive high-density coverage of ion sulfides could restrict the growth of crystal in long range order and cause strain within the lattice. Consequently, the cracking effect is triggered especially on the basal plane and renders the formation of defect-rich sites. Apparently, this cracking effect does not only observed in the study by Xie et al., who use thiourea as sulfur source, but also valid for current study that adopting L-cysteine as sulfur precursor.[23]

The TEM images of the 20 wt%-Ag/MoS_2 nanocomposite are depicted in Fig 3(c) and 3(d). According to Fig. 3(c), the Ag NPs are randomly distributed throughout the surface of MoS_2 nanoflakes, where the pseudo spherical Ag NPs are clearly observed along the edges due to contrast difference. Upon Ag deposition, it is noticed that the MoS_2 nanoflakes underwent slightly structural changes, where it agglomerates with its neighboring sheets. This could be caused by partially removal of the sulfide ions by reducing agent (hydrazine) during decoration process. However, this agglomeration does not significantly diminish the MoS_2 active edges as shown in HRTEM images in Fig 3(d). Meanwhile, the image also reveals that an Ag NP that embedded on the surface of MoS_2 nanoflakes without the sign of continuous film formation. This implies that the Ag NPs does not wet or even diffuse into the lattice of MoS_2 to form alloy, which is in well-agreement with XRD result (Fig. 1(a)). For the samples produced by varying the weight percentage of Ag precursor, it is found that the average size of Ag NPs are strongly depends on the concentration of Ag precursor used. Table 1 depicts the average size that corresponds to the different amount of Ag precursor used. By referring to the table, Ag NPs with larger average size and wide size distribution are produced when higher concentration of Ag precursor is used. This may be due to the excessive agglomeration has taken place as a result of high reactant exchange rate with high concentration of Ag precursor.[25]

Fig. 4(a) shows the HRTEM image of the lattice fringes for both of the Ag NPs and active edges of the MoS_2 nanoflakes, where the difference in the electron scattering have resulted in the distinguishable contrast in between them. As compared to MoS_2 nanoflakes, the Ag NPs that possess high atomic packing density render darker spot due to enhance electron beam scattering. This is further confirmed by its *d*-spacing of 0.23 nm, which belongs to its (111) plane. At the same time, the interlayer spacing of 0.62 nm that belongs to (002) plane of MoS_2 nanoflakes also is observed in the same image. Selected area electron diffraction (SAED) analysis was carried out to further elucidate the crystallinity of the Ag/MoS_2 nanocomposite (Fig. 4(b)). The ring diffraction pattern for MoS_2 appears to be relatively broad and partially diffused, which could be due to the excessively small grain or lower crystallinity.[26] After indexing with the standard JCPDS database for both of Ag and MoS_2, the ring diffraction pattern on the selected area that corresponds to Fig. 4(a) further confirms the coexistence of both of Ag NPs and MoS_2 nanoflakes without the presence of other oxide or sulfide impurities.

Fig. 4 (a) HRTEM image of the 20 wt%-Ag/MoS_2 nanocomposite that depicts the coexistence of both MoS_2 nanoflakes and Ag NPs and the corresponding lattice fringes, (b) ring diffraction pattern of the selected region (red line box) indicates the respective crystal plane of both MoS_2 nanoflakes and Ag NPs, (c) FFT image that projected along [110] zone axis for Ag NPs that embedded onto nanocomposite and (d) FFT image of MoS_2 nanoflakes of 20 wt%-Ag/MoS_2 nanocomposite.

In order to resolve the constituents within the nanocomposite in a much more detail manner, FFT analysis were carried out. Fig. 4(c) depicts the FFT pattern for Ag NPs that can be well-indexed to the standard pattern of Ag with face center cubic phase, which is projected along [110] direction. Additionally, Fig. 4(d) reveals the FFT pattern for MoS_2, where six independent and discontinued

diffraction arcs are clearly shown instead of individual diffraction spot. This implies the MoS_2 nanoflakes do not exist in the form of single crystal with six diffraction spots that are discrete. Instead, the discontinued arcs are due the formation of quasiperiodic structure that arise from the high density of defects.[23]

Fig. 5 (a) Combined signal of 3 elementals (Mo, S, Ag) for 20 wt%-Ag/MoS_2 nanocomposite and (b) the corresponding EDXA spectrum.

The energy dispersive X-ray analysis (EDXA) was conducted to estimate the chemical composition of the 20%-Ag/MoS_2 nanocomposite. It is noticed that the elemental mapping images reveal the presence of Mo and S, which are distributed evenly throughout the sample with Ag alongside (Fig. 5(a)). Fig 5(b) depicts the EDXA spectrum for quantitative analysis of relative atomic percent for each element and the corresponding percentage is summarized in the table. The relative atomic ratio reflects the elemental compositions of the nanocomposite, in which the ratio of Mo: S: Ag is calculated to be 1.2 : 2.9 : 1.0. These values are well-coincide with the resultant area ratio of the elements through XPS analysis.

Fig. 6 UV-vis absorption spectra of commercial MoS_2, MoS_2 nanoflakes, Ag NPs, 5 wt%-Ag/MoS_2, 10 wt%-Ag/MoS_2, 20 wt%-Ag/MoS_2 and 50 wt%-Ag/MoS_2.

Optical absorption spectrum of the MoS_2 nanoflakes (Fig. 6) shows that there is a broad absorption peak centered at about 635 nm. In contrast to other reports, there is not sign of separated A and B exciton peaks are observed.[27, 28] Such discrepancy can be ascribed to the defective nature of the nanoflakes, in which the spin orbits splitting that caused by interlayer interaction are weakened.[29] Also, this sample shows relatively weak absorption beyond the wavelength of 850 nm that can be attributed to the effect of the thinner sheet as

modelled by Li et. al.[2] According to their model (Generalized Gradient Approximation), the surface-state wave function and screening effect of thinner MoS_2 are qualitatively different from that of bulk. As a result, the excitation from the occupied Mo 4d orbital to the unoccupied Mo 4d orbital is symmetrically forbidden beyond 850 nm for thinner MoS_2 nanoflakes, whereas the transition from S 3p to Mo 4d or from Mo 4d to S 3p that make the visible absorption dominant is allowed for this sample. In comparison, the commercial MoS_2 with relatively bulky size exhibits prominent absorption in near IR region but relatively weak absorption in visible region. With such distinguish differences on the absorption between both of these samples, it is therefore deduced that the enhancement of absorption in visible region for the as-synthesized nanoflakes will greatly assist the visible-light driven photocatalytic hydrogen gas production.

Since the photocatalytic performance have direct relationship with optical absorption characteristic, it is crucial to explore the appropriate wt% of Ag to be loaded onto MoS_2 nanoflakes. According to Fig. 6, the decoration of Ag NPs onto MoS_2 nanoflakes has enhanced the visible light absorption for all the nanocomposites, which reflects the unique co-catalyst function of Ag NPs. It is noticed that all the Ag/MoS_2 nanocomposites show absorption peak centered at 606 nm, which are slightly blue-shifted as compared to that of the pure MoS_2 nanoflakes. Moreover, all the nanocomposites also exhibit two small humps that located at 400 nm and 438 nm, which are the characteristic peaks of localized surface plasmon resonance from the Ag NPs. Both of these peaks are due to the collective oscillation of the conduction band electrons after Ag NPs interact with incident visible-light.[30, 31] There is no significant variation on the absorption spectra for all the nanocomposites with different weight percentage of Ag-loading except minor difference in term of absorption intensity.

Fig. 7 Photoluminescence spectra of commercial MoS_2, MoS_2 nanoflakes, 5 wt%-Ag/MoS_2, 10 wt%-Ag/MoS_2 , 20 wt%-Ag/MoS_2 and 50 wt%-Ag/MoS_2.

In general, charge carriers dynamic especially on the aspect of electron-hole separation efficiency has direct influence toward the overall photocatalytic performance. The electron-hole separation efficiency can be correlated with the photoluminescence (PL) emission intensity by taking consideration on the aspect of radiative recombination.[3, 32] Fig. 7 depicts PL emission for the samples that had been excited by using 325 nm He-Cd laser. By referring to the spectra, both of the commercial MoS_2 and MoS_2 nanoflakes exhibit very intense peak centered at 1.81 eV in addition to two noticeable shoulders located at 1.43 eV and 2.15 eV. Both of the peaks (1.81 eV and 2.15 eV) can be assigned to the characteristic peaks of direct-bandgap exciton transition for 2H-MoS_2. According to Mak et al., both of these emissions are caused by direct excitonic transition at the K point of the Brillion zone (K_4-K_5 and K_1-K_5 optical transition, respectively), while the peak with lower energy (1.43 eV) is corresponds to the indirect bandgap transition, which can be ascribed to the as-synthesized nanoflakes that owns thinner sheet in current study.[33]

On the other hand, for all the Ag/MoS_2 nanocomposites, the PL characteristics appear to be quite different if compared to the pure MoS_2, where there are two obvious emissions are observed at 1.81 eV and 1.52 eV in addition to the one that located at 2.15 eV. Interestingly, upon progressive increment of Ag-loading, the intensities of the direct transition (1.81 eV and 2.15 eV) are suppressed while the peak at 1.52 eV is getting pronounced. It is hypothesized that the surface plasmon effect from Ag NPs have led to the suppression of the emission at both of the peaks that located at 1.81 eV and 2.15 eV, in which both of these peaks are generally assigned to be direct transition for MoS_2 [34]. This may be due to the nonradiative decay from the localized plasmonic resonance effect that is contributed by metal NPs have enhanced the numbers of photoexcited electrons. Meanwhile, the enhancement of latter PL peak at 1.52 eV is due to the mechanical strain according to Sun et al.[34], who had conducted the detailed PL analysis on noble metal decorated MoS_2 nanostructures. This is consistent with the report by Pashley et al., [35] who had pointed out that noble metal NPs that partially bind onto MoS_2 can create a stress at the interface between both of the

compounds. In conjunction with this observation, current study also shows that the peak at 1.52 eV seems to exhibit stronger intensity as compared to pure MoS_2 upon the formation of Ag/MoS_2 nanocomposites. Such increment is due to progressively agglomeration in between layers of MoS_2 nanoflakes as a result of partial removal of ion S^{2-} that are anchor on the surface of nanoflakes[36] (by referring to Fig. 3(c)) that would also contribute to the strain as proven by strong surface interaction.

It is noteworthy that the overall PL intensities decrease upon incorporation of Ag NPs, which implies the enhancement in separation efficiency of electron-hole pairs. According to Bhanu et al., who have study the PL quenching in gold-MoS_2 hybrid nanocomposite, they claimed that photoexcited-electrons in higher fermi level showed very high tendency to transfer to its adjacent gold NPs with lower fermi level during illumination.[32] Since gold and Ag are considered to be noble metals that have relatively similar work function and electronic characteristic[37] thus, in current study, the photoexcited-electron is expected to transfer to Ag and hence reduce the recombination rate by decay back to valence band of MoS_2 nanoflakes. With higher loading of Ag NPs onto the surface of MoS_2 nanoflakes, the recombination rate is greatly suppressed, in which the overall PL intensities are largely reduced. Hence, integrating noble metal with semiconductor offers a plausible pathway to promote efficient charge carrier generation.

3.2 Photocatalytic Hydrogen Evolution Activity

Fig. 8 (a) Time-depencence photocatalytic hydrogen gas production profile for Ag NPs, commercial MoS_2, MoS_2 nanoflakes, 5 wt%-Ag/MoS_2, 10 wt%-Ag/MoS_2, 20 wt%-Ag/MoS_2 and 50 wt%-Ag/MoS_2. (b) Yield of hydrogen gas for different samples.

Fig. 8(a) shows the result of visible-light driven photocatalytic hydrogen gas production of pure MoS_2 and nanocomposites. The average hydrogen gas production of commercial MoS_2 is determined to be 92.0 μmol H_2/g_{cat} while that of MoS_2 nanoflakes is 122.5 μmol H_2/g_{cat}. The enhancement in photocatalytic performance of nanoflakes is ascribed to its higher surface area (30.59 m^2/g) with abundance of active sites along the edges if compared to that of commercial MoS_2 (3.96 m^2/g). Moreover, the nanoflakes that appear to be in thinner sheet are well-commensurate with its carrier-diffusion length due to the shorter charge transport pathways from the interior to the solid-water-interface.[38] The complement from both of these factors has strictly promoted redox reaction at the interface between nanoflakes and water for better hydrogen gas evolution rate.

Upon introducing Ag NPs onto MoS_2 nanoflakes, there is obvious improvement on the hydrogen gas evolution rate for all the nanocomposites. The hydrogen gas evolution rates are prevailled after the pure MoS_2 nanoflakes are integrated with co-catalyst Ag NPs. For the sake of clarification, the photocatalytic activity of Ag NPs also was measured under the same condition and it is found out that no any trace amount of H_2 gas being detected upon 5 hours reaction. Therefore, the ability of Ag NPs to trigger the photosensitization process can be excluded and it is clear that the hydrogen gas evolution enhancement is indeed contributed by Ag NPs that serve as co-catalyst.

The enhancement is due to the electron sink effect [39], where Ag NPs can act as a "pool" to gather photoexcited-electrons of MoS_2 nanoflakes and suppress the drawback of recombination. Thereafter, those photoexcited-electrons can be used to trigger photocatalytic reaction in improving hydrogen gas evolution rate. Although UV-vis absorption spectroscopy results indicate that the absorption of Ag/MoS_2 nanocomposites with different Ag-loading does not vary much, however, the hydrogen gas evolution rate appear to be quite different. By referring to Fig. 8(b), the increment of Ag- loading from 5 wt% to 20 wt% (where 20 wt% is identified to be the most optimum condition) has boost up the H_2 gas production rate for 29 %. The result shows that 20 wt% of Ag- loading is the optimum wt% since further topped-up of Ag-loading beyond this level seems to degrade the

photocatalytic performance. The reason lies behind this is due to the formation of larger Ag NPs as a result of excessive agglomeration when higher concentration of Ag precursor is used (Table 1). According to Spinelli et al., the large particles with the size exceeding 30 nm will induced far-field scattering effect, where the incident photons will be scattered away in the form of heat rather than absorbed by the NPs.[40] Moreover, larger size Ag NPs also render additional side effect, in which large portion of incoming photon is blocked along its pathway to reach the active sites of MoS_2. When both of these factors exist, the photoexcited-electrons will be reduced and subsequently lower the numbers of photoexcited-electrons that transfer to Ag NPs. Hence, overall hydrogen gas evolution rate is hampered.

For the sake of comparison, 20-wt% Ag/MoS_2 is selected as a representative sample. It is observed that this sample exhibit almost 46% increment in hydrogen gas production rate (179.5 μmol H_2/g_{cat}) if compared to that of own-synthesized MoS_2 nanoflakes (122.5 μmol H_2/g_{cat}), whereas 95% enhancement is shown if compared to commercial MoS_2 (92.0 μmol H_2/g_{cat}). The enhancement in the hydrogen gas evolution rate is due to efficient transfer of photoexcited charges promoted by Ag NPs co-catalyst. This deduction can be correlated with the PL spectrum (Fig. 7), where all of the nanocomposites exhibit pronounced degradation in PL intensities. The phenomena of lower PL intensities imply that the electron-hole does not undergo recombination by heat dissipation or lattice distortion, which is generally observed.[41] Instead, the photoexcited-electrons manage to diffuse through lattice up to its surface and participate in the redox reaction at the interface between solid and water.

3.3 Photocatalytic Mechanism Discussion

Fig. 9 Schematic represents for visible light hydrogen gas evolution over MoS_2 in the presence of Ag NPs co-catalyst.

The mechanisms that contribute to the enhancement of hydrogen gas evolution rate can be ascribed to the merit of the Ag NPs that serves co-catalyst. Such integration has encouraged the formation of space charge region that will ease the efficient charge separation as illustrated in Fig. 9. Literately have reported that the fermi level of MoS_2 is 4.7-4.0 eV,[32] while the value for Ag NPs is 5.5 eV.[42] Such discrepancy has resulting in a 0.8-1.5 eV of energy level offset, which subsequently causes band bending and the formation of space-charge region at the interface of Ag/MoS_2 nanocomposites system.[32, 43] This region is a charge free region but occupied with a continuum of opposite charges, where MoS_2 side is occupied by negative charges, and Ag co-catalyst side is occupied with positive charges alongside.[44] All the charges are distributed in a parallel manner and are separated with a gap apart.[45] Under thermal equilibrium condition, the dipole as-described above will prevent further movement of the charge carries due to high energy barrier which is resulting by the internal electric field. However, upon irradiation, the thermal equilibrium is perturbed by the incident photons and the electric field in space charge region will strictly promote the photoexcited-electrons to bypass the potential barrier. Thereafter, these electrons will tunnel through the space charge region and gather on the surface of the co-catalyst while holes are left at MoS_2 side. Hence, it is deduced that the formation of space charge region can serve as merit in assisting efficient electron-hole separation and preventing charge recombination.[46] This can be evidenced by obvious PL quenching in the nanocomposites according to PL measurement in Fig. 7, where the integration of Ag co-catalyst have greatly suppress the intensity of PL emission.

As a consequence, if compared to the pure MoS_2, the reduction of water molecules is greatly eased at the surface of Ag NPs that serve as "electron pool" in gathering the photoexcited-electron for further conversion of the hydrogen ions

to H_2 molecules,[47] while oxidation will take place on the active edges of MoS_2 nanoflakes. In order to prevent degradation on the nanocomposites, Na_2S and Na_2SO_3 was adopted as a holes sacrificial agents that is widely used in sulfide-based photocatalyst materials.[48, 49] It is believed that the sulfur ions (S^{2-} and SO_3^{2-}) from Na_2S and Na_2SO_3 provide extra sulfur source to enable surface reconstruction of the MoS_2 as well as prevent further oxidation of MoS_2 nanoflakes.[50-52] Other than that, the sacrificial agents also act as electron donor to react with photo-generated holes,[50] and hence increase the tendency of photo-generated electrons to transfer to the conduction band of the MoS_2 nanoflakes.

This is in well-aggrement with the reports that have been lodged by preceding studies,[53, 54] where incorporation of metal nanoparticles indeed can serve as an alternative route in further enhance the hydrogen gas evolution in water due to fast transfer of the excited electrons generated by photon absorption from the semiconductor to the metal. As a result, undesired recombination by deexcitation to the ground state is strictly-inhibited. Apparently, the contribution of Ag NPs co-catalyst had strictly-promote efficient charge within the nanocomposites if compared to MoS_2 nanoflakes alone.[55] For pure MoS_2 nanoflakes alone, there is a high probability for recombination of excitons to occur.[45, 56, 57]

Conclusions

In summary, Ag/MoS_2 photocatalyst nanocomposite has been successfully synthesized and characterized. The feasibility of the nanocomposite to be used as photocatalyst for visible-light driven hydrogen gas evolution has been tested. The photocatalytic evaluation indicates that hydrogen gas production activities are Ag-loading dependence, where 20 wt%-Ag/MoS_2 shows optimum performance with 95% enhancement in hydrogen gas evolution rate if compared to that of commercial MoS_2 nanopowder. The possible mechanisms that contribute to the enhancement of hydrogen gas evolution rate are proposed, which consisted of synergy effect from semiconductor and Ag co-catalyst. Current study will serve as

a platform to develop efficient nanocomposite photocatalyst by incorporating noble metal co-catalyst on semiconductor for the advancement in renewable energy research.

Acknowledgements

This project was supported by the MOHE-ERGS (ER002-2013A). Additional sources of funding from UMRG (RP007B-13AFR), High Impact Research Program (UM.C/625/1/HIR/079), e-Sciencefund (13-02-03-3093), FRGS (FP038-2014B), HIR-MOHE (UM.C/625/1/HIR/MOHE/SC/06), and Flagship Project Grant (FL017-2011) are also highly appreciated. A. J. Cheah would like to acknowledge Postgraduate Research Fund (PG125-2014B) which is provided by Institute of Research Management and Consultancy (IPPP) of University Malaya.

References

1. K. Rajeshwar, A. Thomas and C. Janáky, *Phys. Chem. Lett.*, 2015, **6**, 139.
2. Y. Li, Y.-L. Li, C. M. Araujo, W. Luo and R. Ahuja, *Catal. Sci. Technol*, 2013, **3**, 2214.
3. L. Ge, C. Han, X. Xiao and L. Guo, *Int. J. Hydrogen Energy*, 2013, **38**, 6960.
4. C.-K. Sun, F. Vallée, L. Acioli, E. Ippen and J. Fujimoto, *Physical Review B*, 1994, **50**, 15337.
5. Y. Yan, B. Y. Xia, Z. Xu and X. Wang, *ACS Catal.*, 2014.
6. Y. Yu, S.-Y. Huang, Y. Li, S. N. Steinmann, W. Yang and L. Cao, *Nano Lett.*, 2014, **14**, 553.
7. J. Li, X. Liu, L. Pan, W. Qin, T. Chen and Z. Sun, *RSC Adv.*, 2014, **4**, 9647.
8. H. J. Conley, B. Wang, J. I. Ziegler, R. F. Haglund Jr, S. T. Pantelides and K. I. Bolotin, *Nano Lett.*, 2013, **13**, 3626.
9. S. Z. Butler, S. M. Hollen, L. Cao, Y. Cui, J. A. Gupta, H. R. Gutierrez, T. F. Heinz, S. S. Hong, J. Huang and A. F. Ismach, *ACS Nano*, 2013, **7**, 2898.

10. X. Zong, G. Wu, H. Yan, G. Ma, J. Shi, F. Wen, L. Wang and C. Li, *J. Phys. Chem. C*, 2010, **114**, 1963.
11. Z. Zou, J. Ye, K. Sayama and H. Arakawa, *Nature*, 2001, **414**, 625.
12. K. P. Jørgensen and J. H. Nielsen, Technical University of DenmarkDanmarks Tekniske Universitet, CenterCenters, Center for Individual Nanoparticle FunctionalityDansk Grundforskningscenter for Individuel Nanopartikel Funktionalitet, 2007.
13. X. Zhang, Y. L. Chen, R.-S. Liu and D. P. Tsai, *Rep. Prog. Phys.*, 2013, **76**, 046401.
14. S. Linic, P. Christopher and D. B. Ingram, *Nat. Mater.*, 2011, **10**, 911.
15. X. Wang, M. Liu, Q. Chen, K. Zhang, J. Chen, M. Wang, P. Guo and L. Guo, *Int. J. Hydrogen Energy*, 2013, **38**, 13091.
16. K.-K. Liu, W. Zhang, Y.-H. Lee, Y.-C. Lin, M.-T. Chang, C.-Y. Su, C.-S. Chang, H. Li, Y. Shi and H. Zhang, *Nano Lett.*, 2012, **12**, 1538.
17. Y. Tian, Y. He and Y. Zhu, *Mater. Chem. Phys.*, 2004, **87**, 87.
18. W. Chiu, S. Radiman, R. Abd-Shukor, M. Abdullah and P. Khiew, *J. Alloys Compd.*, 2008, **459**, 291.
19. T. Weber, J. Muijsers and J. Niemantsverdriet, *J. Phys. Chem.*, 1995, **99**, 9194.
20. X. Xia, X. Zhao, W. Ye and C. Wang, *Electrochim. Acta*, 2014, **142**, 173.
21. K. Asami, *J. Electron. Spectrosc. Relat. Phenom.*, 1976, **9**, 469.
22. D. Kong, H. Wang, J. J. Cha, M. Pasta, K. J. Koski, J. Yao and Y. Cui, *Nano Lett.*, 2013, **13**, 1341.
23. J. Xie, H. Zhang, S. Li, R. Wang, X. Sun, M. Zhou, J. Zhou, X. W. D. Lou and Y. Xie, *Adv. Mater.*, 2013, **25**, 5807.
24. L. Yang, S. Wang, J. Mao, J. Deng, Q. Gao, Y. Tang and O. G. Schmidt, *Adv. Mater.*, 2013, **25**, 1180.
25. Y.-S. Chi, H.-P. Lin and C.-Y. Mou, *Appl. Catal., A*, 2005, **284**, 199.
26. W.-H. Ryu, J.-W. Jung, K.-S. Park, S. Kim and I.-D. Kim, *Nanoscale*, 2014.
27. G. Eda, H. Yamaguchi, D. Voiry, T. Fujita, M. Chen and M. Chhowalla, *Nano Lett.*, 2011, **11**, 5111.

28. B. Visic, R. Dominko, M. K. Gunde, N. Hauptman, S. D. Skapin and M. Remskar, *Nanoscale Res. Lett.*, 2011, **6**, 1.
29. G. Frey, S. Elani, M. Homyonfer, Y. Feldman and R. Tenne, *Phys. Rev. B: Condens. Matter*, 1998, **57**, 6666.
30. A. Slistan-Grijalva, R. Herrera-Urbina, J. F. Rivas-Silva, M. Ávalos-Borja, F. F. Castillón-Barraza and A. Posada-Amarillas, *Mater. Res. Bull.*, 2008, **43**, 90.
31. N. R. Jana, L. Gearheart and C. J. Murphy, *Chem. Commun.*, 2001, 617.
32. U. Bhanu, M. R. Islam, L. Tetard and S. Khondaker, *Sci. Rep.*, 2014.
33. K. F. Mak, C. Lee, J. Hone, J. Shan and T. F. Heinz, *Phys. Rev. Lett.*, 2010, **105**, 136805.
34. Y. Sun, K. Liu, X. Hong, M. Chen, J. Kim, S. Shi, J. Wu, A. Zettl and F. Wang, *Nano Lett.*, 2014, **14**, 5329.
35. D. Pashley, M. Stowell, M. Jacobs and T. Law, *Philos. Mag.*, 1964, **10**, 127.
36. A. Krivosheeva, V. Shaposhnikov, V. Borisenko and J.-L. Lazzari, *Anon*, 2014.
37. M. Uda, A. Nakamura, T. Yamamoto and Y. Fujimoto, *J. Electron. Spectrosc. Relat. Phenom.*, 1998, **88–91**, 643.
38. F. E. Osterloh, *J. Phys. Chem. Lett.*, 2014, **5**, 2510.
39. P. Sangpour, F. Hashemi and A. Z. Moshfegh, *J. Phys. Chem. C*, 2010, **114**, 13955.
40. P. Spinelli and A. Polman, *Opt. Express*, 2012, **20**, A641.
41. U. Bhanu, M. R. Islam, L. Tetard and S. I. Khondaker, *Sci. Rep.*, 2014, **4**.
42. L. Baia, M. Baia, W. Kiefer, J. Popp and S. Simon, *Chemical physics*, 2006, **327**, 63.
43. M. Farmanbar and G. Brocks, *Phys. Rev. B: Condens. Matter*, 2015.
44. C. P. Poole Jr, *Encyclopedic Dictionary of Condensed Matter Physics*, Academic Press, 2004.
45. T. Torimoto, H. Horibe, T. Kameyama, K.-i. Okazaki, S. Ikeda, M. Matsumura, A. Ishikawa and H. Ishihara, *The Journal of Physical Chemistry Letters*, 2011, **2**, 2057.

46. A. Bumajdad and M. Madkour, *PCCP*, 2014, **16**, 7146.
47. A. Fujishima, T. N. Rao and D. A. Tryk, *J. Photochem. Photobiol., C*, 2000, **1**, 1.
48. J. Zhang, J. Yu, Y. Zhang, Q. Li and J. R. Gong, *Nano Lett.*, 2011, **11**, 4774.
49. J. B. Joo, R. Dillon, I. Lee, Y. Yin, C. J. Bardeen and F. Zaera, *Proceedings of the National Academy of Sciences*, 2014, **111**, 7942.
50. J. Schneider and D. W. Bahnemann, *J. Phys. Chem. Lett.*, 2013, **4**, 3479.
51. A. Roy and G. De, *J. Photochem. Photobiol., A*, 2003, **157**, 87.
52. N. Li, M. Liu, Z. Zhou, J. Zhou, Y. Sun and L. Guo, *Nanoscale*, 2014, **6**, 9695.
53. I. Lee, J. B. Joo, Y. Yin and F. Zaera, *Angewandte Chemie*, 2011, **123**, 10390.
54. X. Chen, S. Shen, L. Guo and S. S. Mao, *Chemical Reviews*, 2010, **110**, 6503.
55. K. Awazu, M. Fujimaki, C. Rockstuhl, J. Tominaga, H. Murakami, Y. Ohki, N. Yoshida and T. Watanabe, *J. Am. Chem. Soc.*, 2008, **130**, 1676.
56. F. Wang, P. Stepanov, M. Gray and C. N. Lau, *Nanotechnology*, 2015, **26**, 105709.
57. E. A. Rozhkova and K. Ariga, *From Molecules to Materials: Pathways to Artificial Photosynthesis*, Springer, 2015.

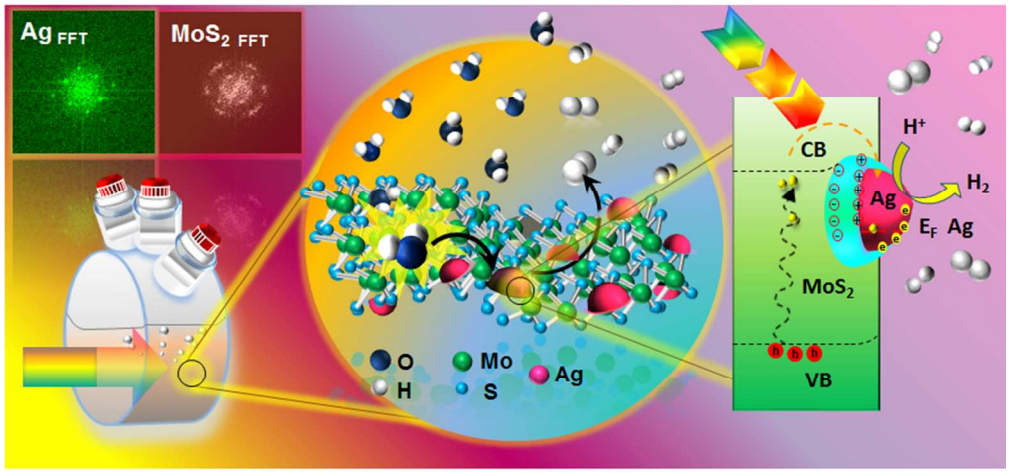

Schemetic diagram of visible light driven hydrogen gas generation on the surface of Ag/MoS_2 nanocomposite system.
233x109mm (96 x 96 DPI)

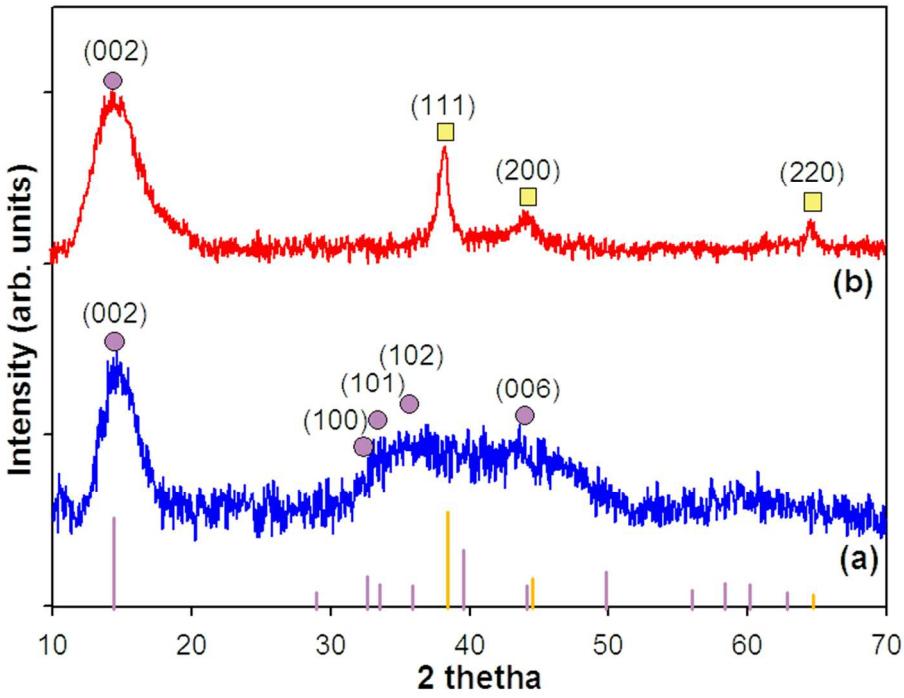

Fig. 1 XRD patterns of the (a) as-synthesized MoS_2 nanoflakes and (b) 20 wt %-Ag/MoS_2 nanocomposite. (The darkviolet and khaki-solid line at the bottom refers to the standard pattern of MoS_2 and Ag, respectively).
149x123mm (150 x 150 DPI)

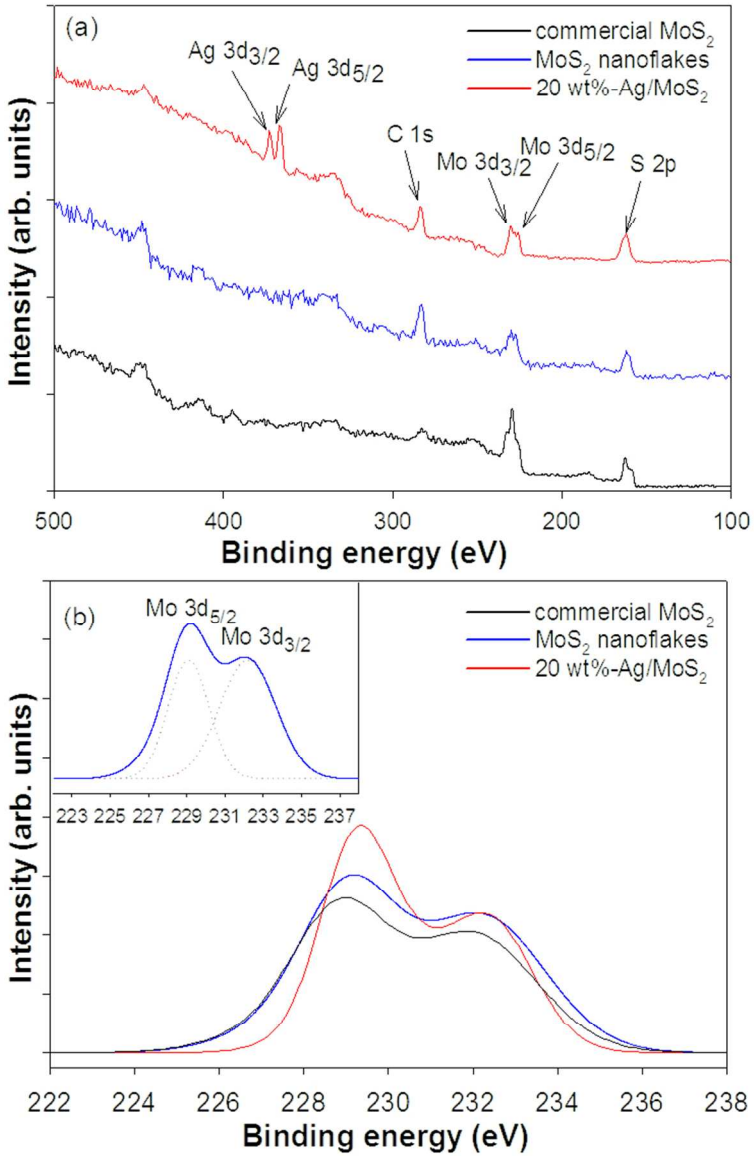

Fig. 2 (a) Wide scan for the commercial MoS_2 nanopowder, MoS_2 nanoflakes and 20 wt%-Ag/MoS_2 nanocomposite (b) narrow scan for the Mo 3d inset of Fig2b is the resolved spectra after deconvoluted to its constituent state).
64x99mm (300 x 300 DPI)

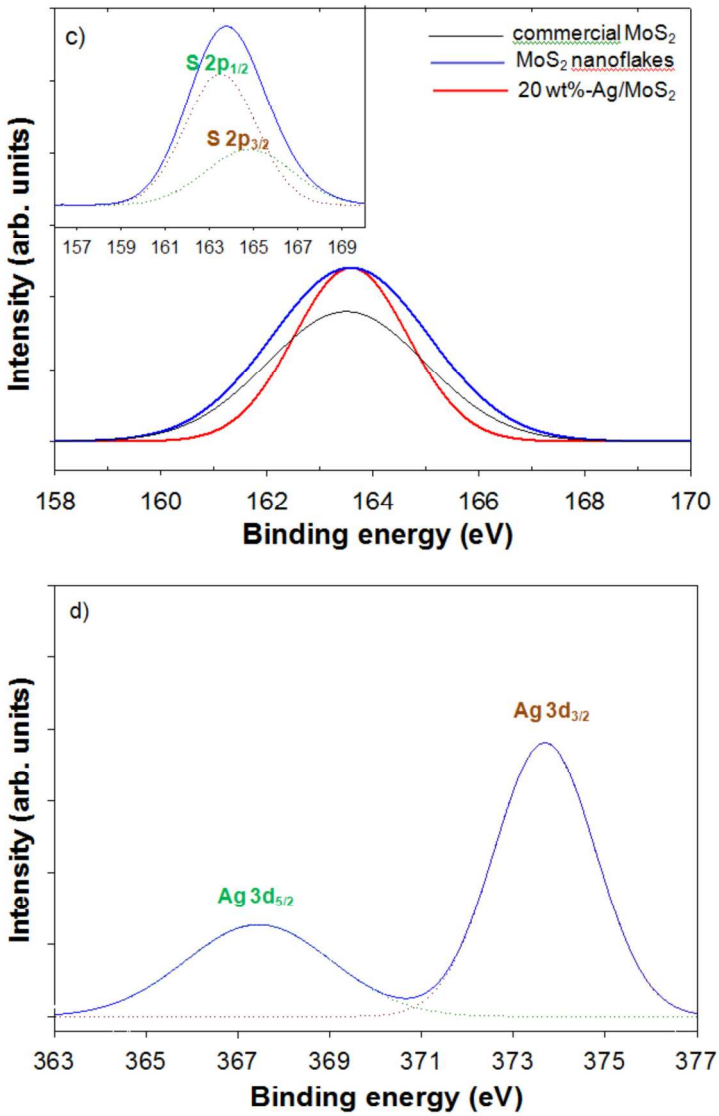

Fig. 2 (a) Wide scan for the commercial MoS_2 nanopowder, MoS_2 nanoflakes and 20 wt%-Ag/MoS_2 nanocomposite (b) narrow scan for the Mo 3d, (c) S 2p and (d) Ag 3d (insets of Fig. 2(b) and 2(c) are the resolved spectra after deconvoluted to its constituent state).
289x431mm (300 x 300 DPI)

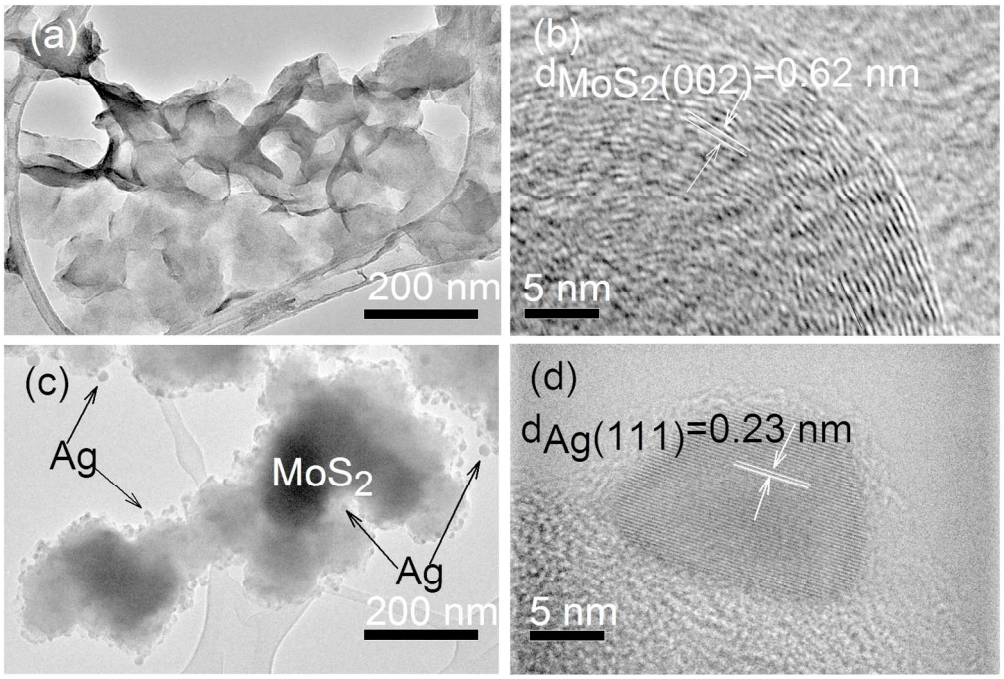

Fig. 3 (a) Low magnification (30k ×) TEM image of MoS_2 nanoflakes that was suspended on lacey copper grid. (b) High resolution TEM image (800k ×) of MoS_2 nanoflakes that depicts the defect-rich active edges with discontinued microstructures. (c) Low magnification (30k ×) TEM image of 20 wt%-Ag/MoS_2 nanocomposite reveals that Ag NPs are randomly distributed onto MoS_2 nanoflakes. (d) High resolution TEM image (800k ×) of the Ag NPs that embedded on the MoS_2 nanoflakes.
148x99mm (300 x 300 DPI)

Table 1

Samples	Average size of Ag NPs (nm)
5 wt%-Ag/MoS_2	12.7
10 wt%-Ag/MoS_2	13.8
20 wt%-Ag/MoS_2	18.9
50 wt%-Ag/MoS_2	51.1

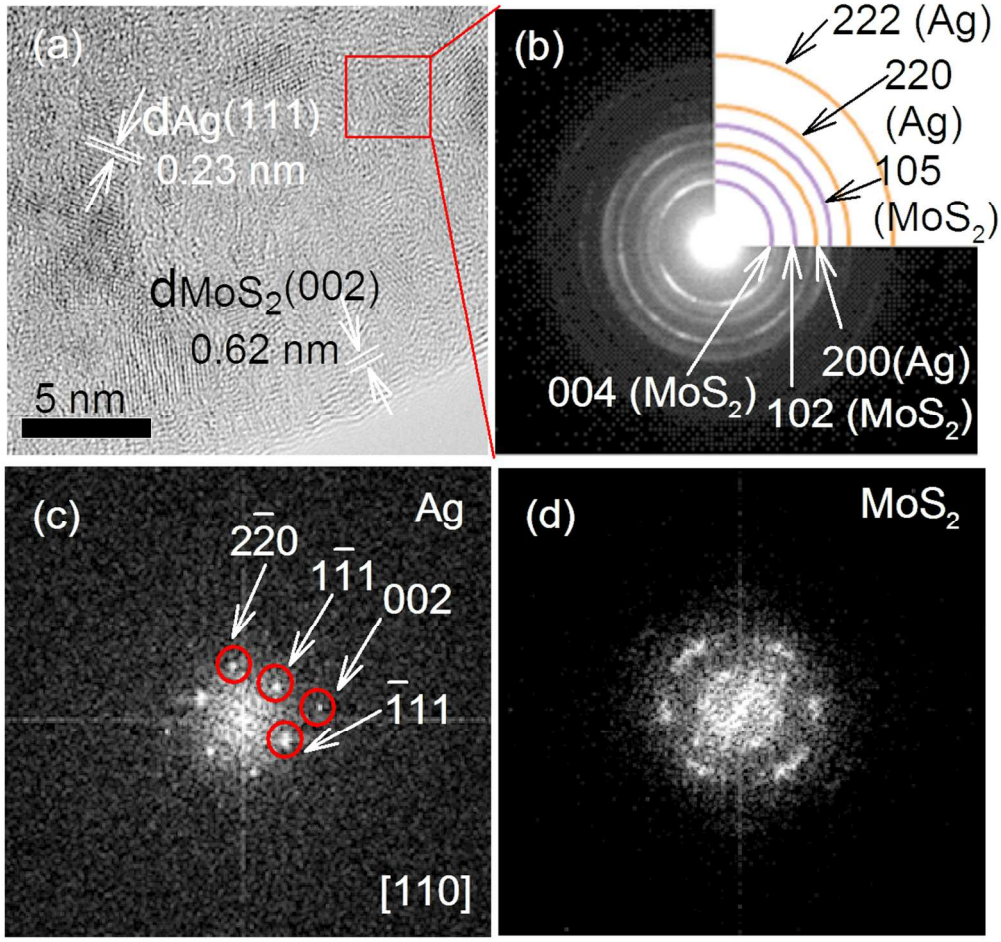

Fig. 4 (a) HRTEM image of 20 wt%-Ag/MoS_2 nanocomposite depicts the coexistence of both MoS_2 nanoflakes and Ag NPs and the corresponding lattice fringes, (b) ring diffraction pattern of the selected region (red line box) indicates the respective crystal plane of both MoS_2 nanoflakes and Ag NPs, (c) FFT image along [110] zone axis for Ag NPs that embedded onto nanocomposite and (d) FFT image of MoS_2 nanoflakes of 20 wt%-Ag/MoS_2 nanocomposite.
105x99mm (300 x 300 DPI)

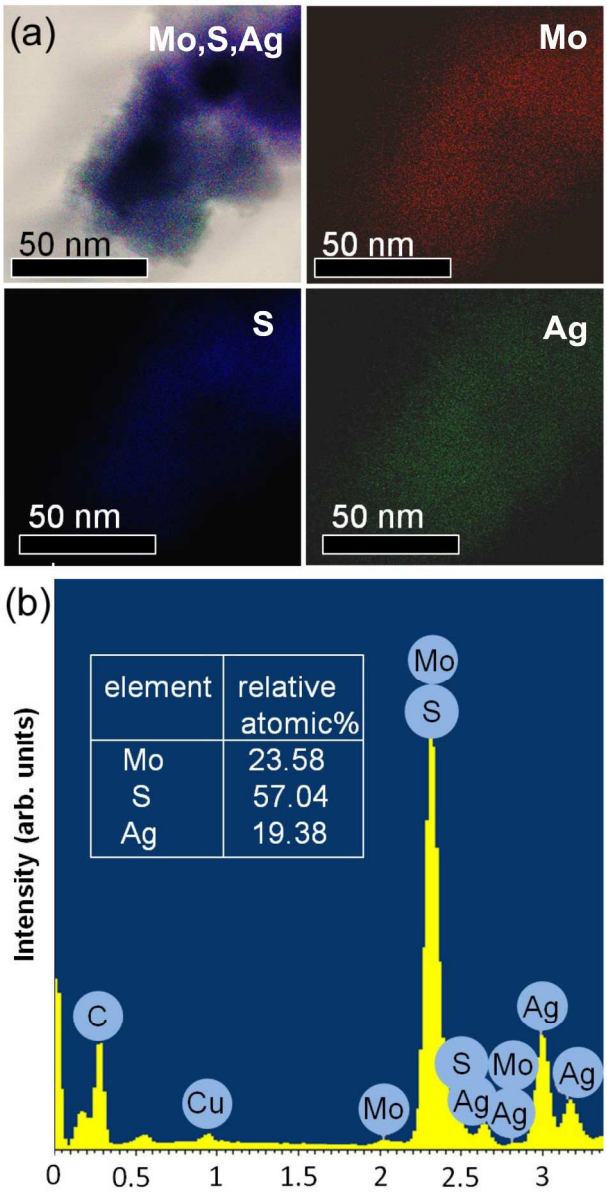

Fig. 5 (a) Combined signal of 3 elementals (Mo, S, Ag) for 20 wt%-Ag/MoS_2 nanocomposite and (b) the corresponding EDXA spectrum.
194x374mm (300 x 300 DPI)

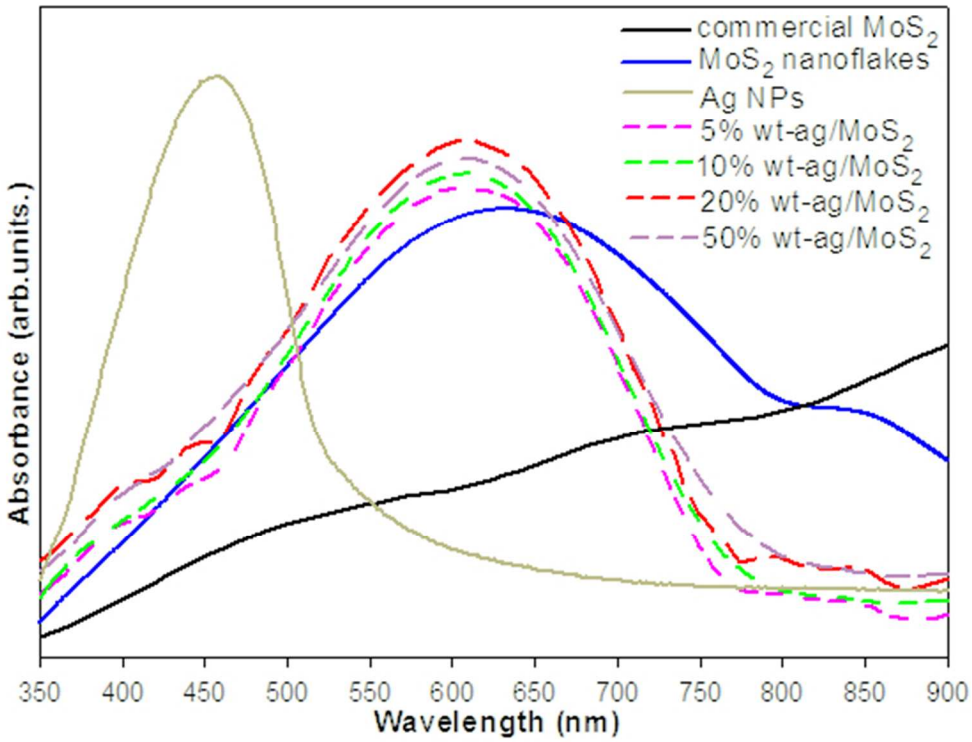

Fig. 6 UV-vis absorption spectra of commercial MoS_2, MoS_2 nanoflakes, Ag nanoparticles, 5 wt%-Ag/MoS_2, 10 wt%-Ag/MoS_2, 20 wt%-Ag/MoS_2, 50 wt%-Ag/MoS_2.
48x39mm (300 x 300 DPI)

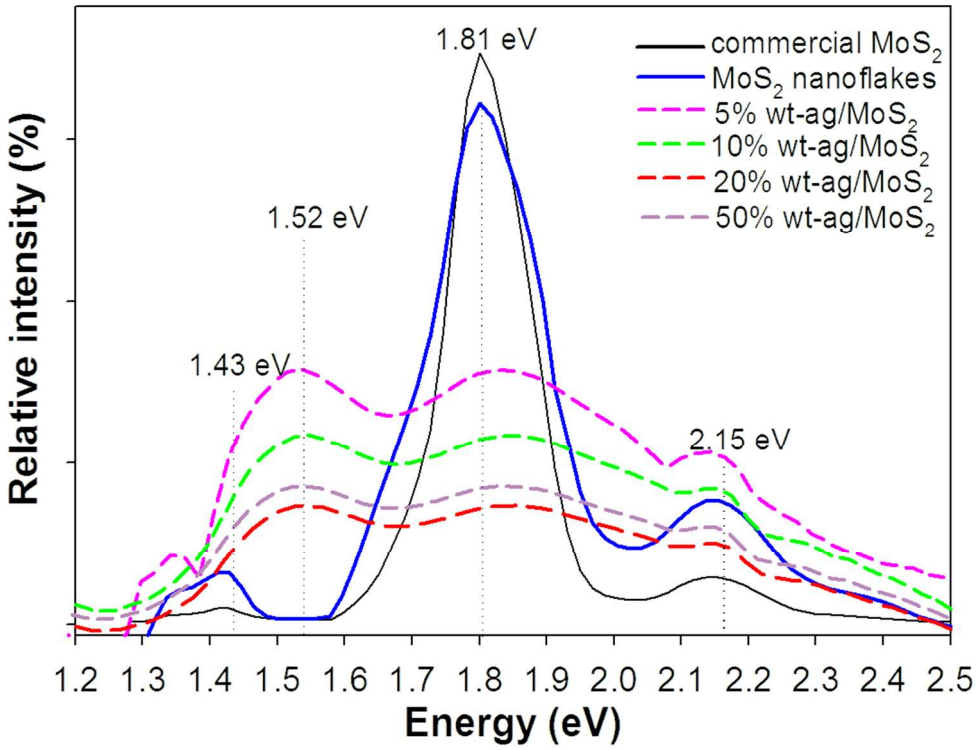

Fig. 7 Photoluminescence spectra of commercial MoS_2, MoS_2 nanoflakes, 5 wt%-Ag/MoS_2, 10 wt%-Ag/MoS_2, 20 wt%-Ag/MoS_2 and 50 wt%-Ag/MoS_2.
93x80mm (300 x 300 DPI)

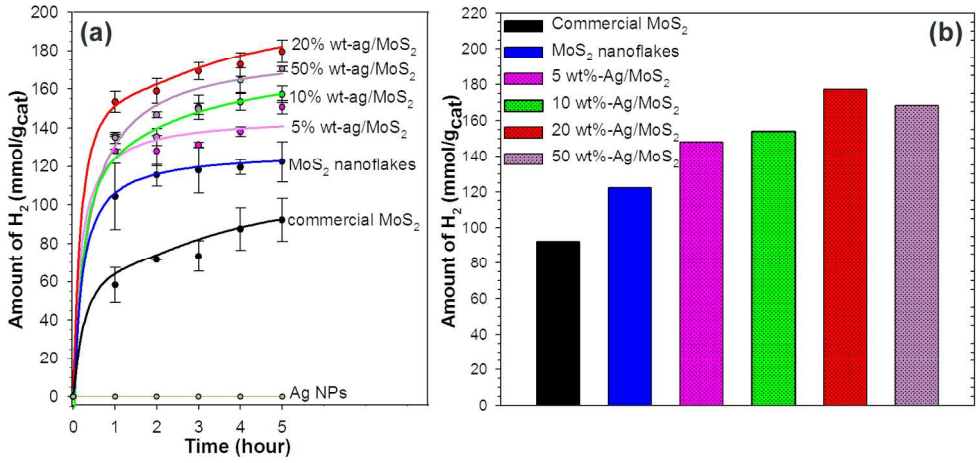

Fig. 8 (a) Time-depencence photocatalytic hydrogen gas production profile for Ag NPs, commercial MoS_2, MoS_2 nanoflakes, 5 wt%-Ag/MoS_2, 10 wt%-Ag/MoS_2, 20 wt%-Ag/MoS_2 and 50 wt%-Ag/MoS_2. (b) Yield of hydrogen gas for different samples.
159x80mm (300 x 300 DPI)

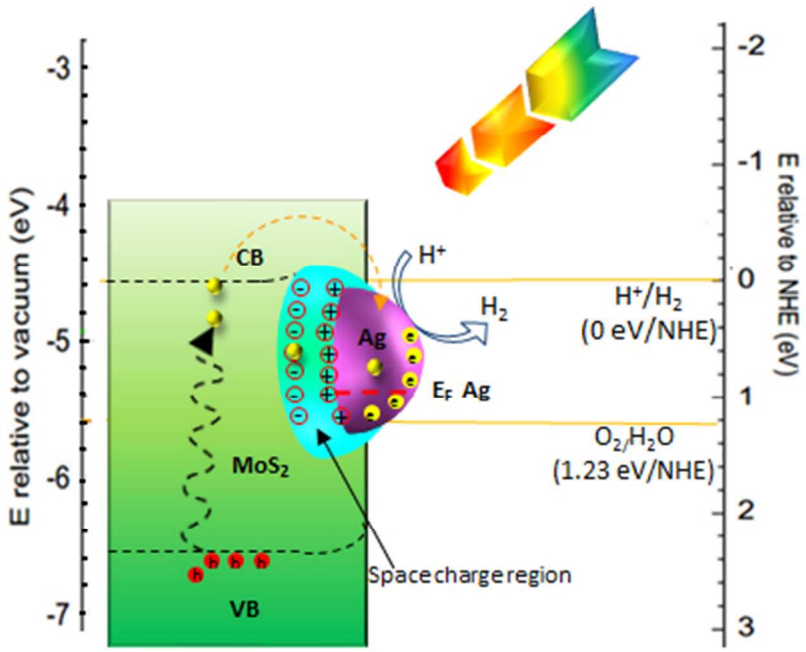

Fig. 9 Schematic represents for visible light hydrogen gas evolution over MoS_2 in the presence of Ag NPs co-catalyst.
107x86mm (96 x 96 DPI)